Nanoscale

Halide Exchange Mediated Cation Exchange Facilitates Room Temperature Co-doping of d-and f-Block Elements in Cesium Lead Halide Perovskite Nanoparticles

Journal:	*Nanoscale*
Manuscript ID	NR-ART-02-2024-000805.R1
Article Type:	Paper
Date Submitted by the Author:	01-Apr-2024
Complete List of Authors:	Philip, Jomy Jose; Jain University, Centre for Nano and Material Sciences Debnath, Gouranga; Jain University, Centre for Nano and Material Sciences Waldeck, David; University of Pittsburgh, Department of Chemistry Balakrishna, R.; Jain University, Centre for Nano and Material Sciences

Halide Exchange Mediated Cation Exchange Facilitates Room Temperature Co-doping of d-and f-Block Elements in Cesium Lead Halide Perovskite Nanoparticles

Jomy Jose Philip,[1] Gouranga H. Debnath,[1]* David H. Waldeck,[2,3]* and R. Geetha Balakrishna,[1]*

[1]Centre for Nano and Material Sciences, Jain University, Bangalore, Karnataka 562112, India

[2]Department of Chemistry, University of Pittsburgh, Pittsburgh, Pennsylvania 15260, USA

[3]Petersen Institute of NanoScience and Engineering, University of Pittsburgh, Pittsburgh, Pennsylvania 15261, USA

E-mail:gouranga.debnath@jainuniversity.ac.in, gouranga0430gmail.com (Gouranga H. Debnath)

dave@pitt.edu (David H. Waldeck)

br.geetha@jainuniversity.ac.in (R. Geetha Balakrishna)

*To whom the correspondence should be addressed

Keywords: Lanthanides, Manganese, Perovskites, Nanoparticles, Ion Exchange, Co-doping

Abstract: This study presents a halide exchange mediated cation exchange reaction to co-dope d- and f-block elements in $CsPbX_3$ NPs at room temperature. Addition of $MnCl_2$ and $YbCl_3$ to $CsPbBr_3$ NPs induces ion exchange reactions generating the corresponding $CsPbBr_3/MnCl_2YbCl_3$ NPs. In addition to the perovskite emission, the NPs display sensitized Mn^{2+} and Yb^{3+} emissions in concert spanning the UV, visible, and NIR spectral region. Structural and spectroscopic characterizations indicate a substitutional displacement of Pb^{2+} by the Mn^{2+} and Yb^{3+}. The identity of the host halide in modulating the ion exchange reactions was also tested. An effective perovskite host NP is presented that can be used to incorporate d-f or f-f dopant combinations to realize a gamut of dopant emission lines. A charge trapping based photophysical model is developed that focuses on rational energy alignments to predict dopant emissions semi-empirically and aids the design of optimal perovskite host–multi-dopant combinations.

Introduction: Generating multicolor emission from cesium lead halide ($CsPbX_3$, where X = Cl, Br, or I) perovskite nanoparticles (NPs) has garnered huge attention in the past six years because of their potential applications for next generation photovoltaics, sensors, light emitting diodes (LEDs), lasers, and optoelectronics.[1-5] This interest arises from the high defect tolerance[6] exhibited by the $CsPbX_3$ NPs (when compared to conventional semiconductors), their near unity emission quantum yields[7] (in cases), high absorption cross-section,[8] and tunable exciton emission bands through the modulation of either halide composition and/or quantum confinement.[9-11]

The introduction of multiple emission centers in the perovskite lattice by co-doping transition metal ions and/or trivalent lanthanide ions (Ln^{3+}) (typically achieved by tuning the Pb^{2+} to dopant(s) ratio during the synthesis of $CsPbX_3$ NPs) has been achieved and gives rise to multicolor emission.[12] By choice of the transition metal ions and the sharp, non-overlapping emissions of the Ln^{3+} dopants, one can generate materials with a series of well-defined emission bands that span the entire visible and near infrared spectral region.[13-15] Additionally, the long emission lifetimes of these ions (in the range of microseconds to milliseconds) and resistance to photobleaching are superior to traditional organic fluorophores.[14, 16, 17] In 2017, Song and coworkers reported the synthesis of Yb^{3+}, Ce^{3+} co-doped $CsPbCl_{1.5}Br_{1.5}$ NPs.[18] By modulating the Yb^{3+} and Ce^{3+} emissions to generate effective downconverters through quantum cutting, they improved the photoelectric conversion efficiency of silicon solar cells from 18.1% to 21.5%. Later, Song's group also reported the realization of white light emission from Bi^{3+} and Mn^{2+} co-doped $CsPbCl_3$ NPs.[19] Yu and coworkers reported the synthesis of Yb^{3+} and Er^{3+} co-doped $CsPbCl_3$ NPs and concluded that the suppression of the defect states by the incorporation of Yb^{3+} helped in promoting the Er^{3+} emission at 1.5 μm for applications in telecommunications.[20] In 2021, Artizzu and coworkers presented a direct synthetic strategy to generate Mn^{2+}-Ln^{3+} co-doped $CsPbCl_3$ NPs

[Ln^{3+} = Nd, Ho, and Er] where the Mn^{2+} donor was used to trigger the near infrared (NIR) emissions in the Ln^{3+}.[21] These works illustrate the benefits and new properties that can arise from controlled doping of NPs.

In this work we demonstrate how a post-synthetic modification of undoped NPs, can be used to incorporate transition metals ions and/or Ln^{3+} in $CsPbX_3$ NPs.[14] Although literature reports on a post-synthetic doping mechanism to incorporate a single emitter species in traditional semiconductor NPs[14, 22, 23] and recently $CsPbX_3$ NPs[24, 25] exist, cases dealing with the post-synthetic co-doping in metal halide perovskite NPs has remained elusive. This work introduces a facile halide exchange mediated cation exchange (HEMCE) reaction to co-dope Mn^{2+} and Yb^{3+} ions post-synthetically into three-dimensional, quantum confined $CsPbBr_3$ and $CsPbCl_3$ NPs at room temperature to generate the corresponding $CsPbBr_3/MnCl_2YbCl_3$ NPs and $CsPbCl_3/MnCl_2YbCl_3$ NPs (see **Scheme 1**). The performance of the perovskite NPs in sensitizing the Mn^{2+} and Yb^{3+} emission is evaluated. The generality of the HEMCE reaction is tested with a Eu^{3+}–Tb^{3+} co-dopant combination in $CsPbCl_3$ NPs. The selection of the Mn^{2+}–Yb^{3+} and Eu^{3+}–Tb^{3+} combinations are guided by (i) the presence of a single major luminescent energy level present in these ions, (ii) the fact that Tb^{3+} and Eu^{3+} display the brightest visible emission bands for the Ln^{3+} series, and (iii) the possibility to access emission lines spanning the UV, visible, and NIR region.[26-28] Additionally, we propose a photophysical framework that helps predict the success of sensitized dopant(s) emission and can be used to guide the design of perovskite-dopant(s) host-guest(s) combinations.[14] The post-synthetic co-doping strategy allows multiplexing[29, 30] and helps to compare the dopant induced photophysical and structural changes in the doped vs undoped NPs with the undoped NPs acting as an internal control. Also, a single batch of undoped NPs can be used to generate multiple batches of doped NPs with distinct dopant

densities and/or combinations thereby circumventing the pitfalls of synthetic heterogeneity that arises from multiple direct syntheses of co-doped perovskite NPs.

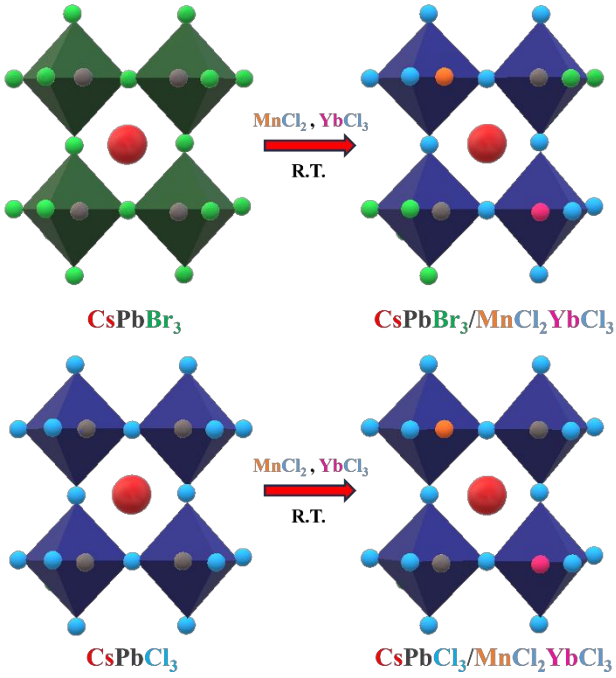

Scheme 1. The transformation of $CsPbBr_3$ and $CsPbCl_3$ NPs to $CsPbBr_3/MnCl_2YbCl_3$ and $CsPbCl_3/MnCl_2YbCl_3$ NPs respectively on post-synthetic addition of $MnCl_2$ and $YbCl_3$ via the HEMCE reaction is shown.

Results and Discussion

HEMCE and Co-doping Mn^{2+}, Yb^{3+}

The $CsPbBr_3$ NPs were synthetized according to standard literature protocol[9] (see Experimental Section for details). **Figure 1a** shows the high-resolution transmission electron microscopy (HRTEM) image of the $CsPbBr_3$ NPs, which apart from a cubic morphology display d-spacings of 0.29 nm and 0.41 nm that correlate to the (220) and (020) planes of orthorhombic $CsPbBr_3$ respectively (note the average particle edge length of 6.3 ± 0.6 nm in $CsPbBr_3$ NPs as shown in **Figure S1**). The X-ray diffraction (XRD) pattern of the $CsPbBr_3$ NPs shown in **Figure 1c** further corroborates this claim with peaks at $2\theta = 15^o$, 21.2^o, 30.4^o, 34.1^o, 37.5^o, and 43.5^o which conform to the (110), (020), (220), (130), (312), and (224) planes of orthorhombic $CsPbBr_3$ respectively

(PDF: 01-072-7929).[25] Addition of $MnCl_2$ and $YbCl_3$ salts to the $CsPbBr_3$ NPs induces a simultaneous halide and cation exchange (*vide infra*). The halide exchange preserves the overall cubic morphology and dimension of the NPs (with an average particle edge length of 6.4 ± 0.5 nm see **Figure S1**) but changes the d-spacings of the resulting $CsPbBr_3/MnCl_2YbCl_3$ NPs to 0.28 nm and 0.39 nm which correspond to the (200) and (110) planes of cubic $CsPbCl_3$ respectively as shown in the HRTEM image in **Figure 1b**.

Further evidence for the progression of the halide exchange is evident from the marked shift in the XRD pattern of the $CsPbBr_3/MnCl_2YbCl_3$ NPs (when compared to the $CsPbBr_3$ NPs) with peaks at $2\theta = 15.5^o$, 22.0^o, 31.4^o, 35.2^o, 38.8^o, and 45.1^o which nearly overlap with the (100), (110), (200), (210), (211), and (220) planes of cubic $CsPbCl_3$ (PDF:01-073-0692) (see **Figure 1d**).[25] This near overlap of the $CsPbBr_3/MnCl_2YbCl_3$ XRD peaks with those of standard cubic $CsPbCl_3$ indicate a nearly complete halide exchange[10] and becomes apparent from later discussions.

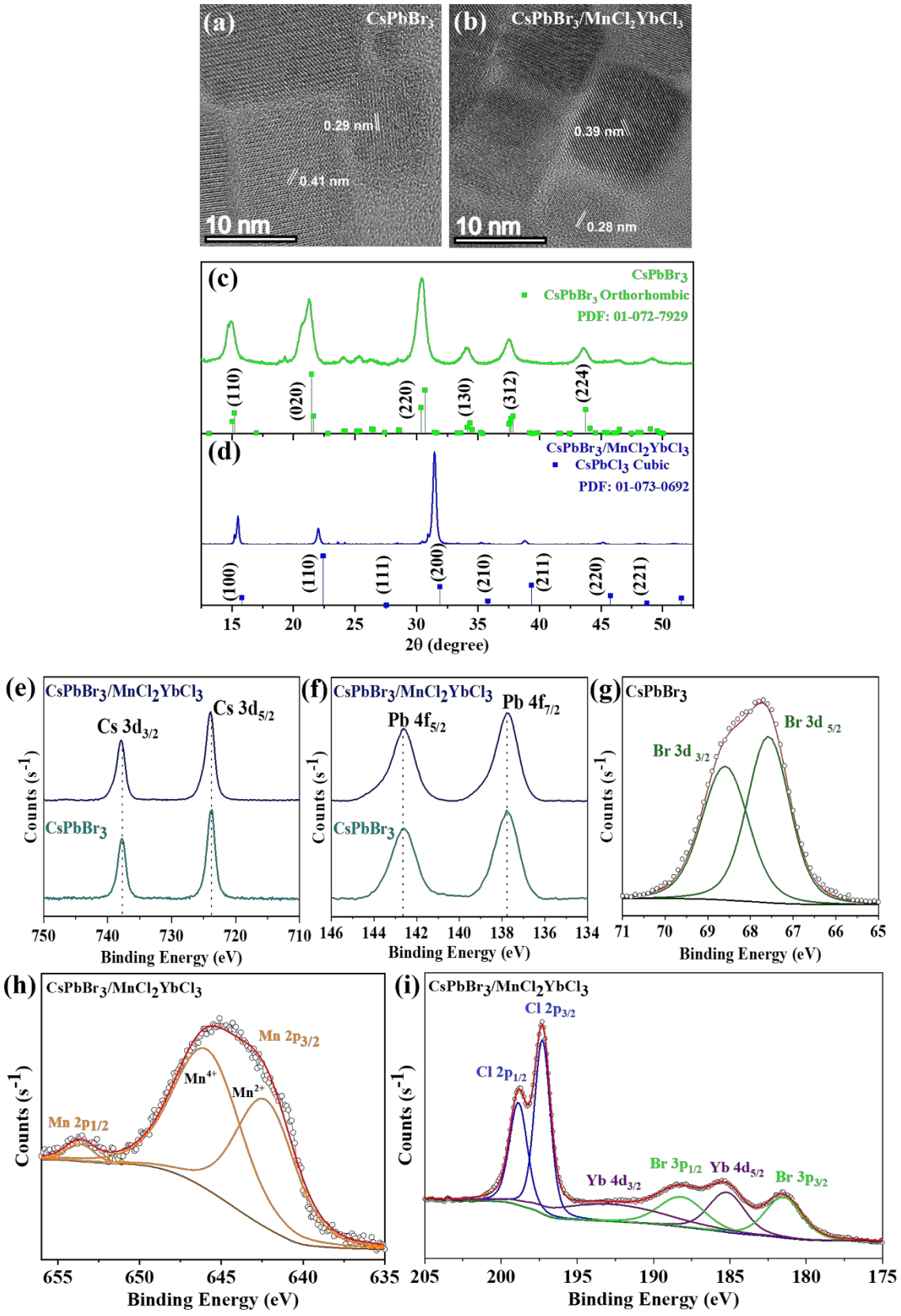
(a)
CsPbBr3
0.29 nm
0.41 nm
10 nm
(b)
CsPbBr3/MnCl2YbCl3
0.39 nm
0.28 nm
10 nm
(c)
CsPbBr3
CsPbBr3 Orthorhombic
PDF: 01-072-7929
(110)
(020)
(220)
(130)
(312)
(224)
(d)
CsPbBr3/MnCl2YbCl3
CsPbCl3 Cubic
PDF: 01-073-0692
(100)
(110)
(111)
(200)
(210)
(211)
(220)
(221)
15 20 25 30 35 40 45 50
2θ (degree)
(e)
CsPbBr3/MnCl2YbCl3
Cs 3d3/2
Cs 3d5/2
CsPbBr3
Counts (s-1)
750 740 730 720 710
Binding Energy (eV)
(f)
CsPbBr3/MnCl2YbCl3
Pb 4f5/2
Pb 4f7/2
CsPbBr3
Counts (s-1)
146 144 142 140 138 136 134
Binding Energy (eV)
(g)
CsPbBr3
Br 3d 3/2
Br 3d 5/2
Counts (s-1)
71 70 69 68 67 66 65
Binding Energy (eV)
(h)
CsPbBr3/MnCl2YbCl3
Mn 2p3/2
Mn4+
Mn2+
Mn 2p1/2
Counts (s-1)
655 650 645 640 635
Binding Energy (eV)
(i)
CsPbBr3/MnCl2YbCl3
Cl 2p3/2
Cl 2p1/2
Yb 4d3/2
Br 3p1/2
Yb 4d5/2
Br 3p3/2
Counts (s-1)
205 200 195 190 185 180 175
Binding Energy (eV)

Figure 1. High-resolution TEM images of the (a) $CsPbBr_3$ and (b) $CsPbBr_3/MnCl_2YbCl_3$ NPs are shown along with XRD patterns of the (c) $CsPbBr_3$ (green) and (d) $CsPbBr_3/MnCl_2YbCl_3$ NPs (blue). The powder diffraction files (PDF) of orthorhombic $CsPbBr_3$ and cubic $CsPbCl_3$ are also presented to facilitate appropriate comparison. XPS data of (e) Cs 3d and (f) Pb 4f of $CsPbBr_3$ (dark cyan) and $CsPbBr_3/MnCl_2YbCl_3$ NPs (navy) are shown along with (g) Br 3d spectra (fitted in olive) of the $CsPbBr_3$ NPs. The XPS of (h) Mn 2p (fitted in orange) and (i) Yb 4d with fits (purple) along with Cl 2p and Br 3p (fitted in blue and green respectively) are shown in panel (i) for the $CsPbBr_3/MnCl_2YbCl_3$ NPs. Through panels (g-i), the spectra are presented as black circles while the envelope of the fit is shown with a red line.

Figures 1(e-f) compares the X-ray photoelectron spectroscopy (XPS) data of Cs 3d ($3d_{3/2}$ and $3d_{5/2}$ doublet) and Pb 4f ($4f_{5/2}$ and $4f_{7/2}$ doublet) of the $CsPbBr_3$ NPs and the $CsPbBr_3/MnCl_2YbCl_3$ NPs. The minor core level shifts (as indicated by dotted lines) in the Cs 3d and Pb 4f spectra between the undoped ($CsPbBr_3$) and the $CsPbBr_3/MnCl_2YbCl_3$ NPs correlate to a change in the electron density and is a result of doping.[31] **Figure 1g** shows the Br 3d ($3d_{3/2}$ and $3d_{5/2}$ doublet) spectra of the $CsPbBr_3$ NPs (note the presence of Br 3d signatures also in $CsPbBr_3/MnCl_2YbCl_3$ NPs, **see Figure S2**).[25] The post-synthetic halide exchange and the incorporation of the Mn^{2+} and Yb^{3+} into the perovskite framework is further substantiated from **Figure 1h** which shows the Mn 2p ($2p_{1/2}$ and $2p_{3/2}$ doublet) spectra of the $CsPbBr_3/MnCl_2YbCl_3$ NPs.[31, 32] Some contribution of the Mn^{4+} is also noted and is consistent with similar literature treatments on Mn^{2+} doped $CsPbX_3$ NPs.[33, 34] The shifts in the binding energy of the Mn $2p_{1/2}$ and $2p_{3/2}$ doublet in the $CsPbBr_3/MnCl_2YbCl_3$ NPs when compared to the $MnCl_2$ salt further underscores the change in the electronic density of the Mn^{2+} in the doped case (**see Figure S2**). **Figure 1h** shows a binding energy range in $CsPbBr_3/MnCl_2YbCl_3$ NPs constituting overlapping bands that have been assigned to the Cl 2p ($2p_{1/2}$ and $2_{p3/2}$ doublet), Yb 4d ($4d_{3/2}$ and $4_{d5/2}$ doublet), and Br 3p ($3p_{1/2}$ and $3p_{3/2}$).[35] The presence of Br XPS signatures corroborates the results of the XRD for $CsPbBr_3/MnCl_2YbCl_3$ NPs which argues a near completion of the halide exchange reaction (*vide supra*). The presence of the Mn 2p and Yb 4d signatures in the XPS data of the $CsPbBr_3/MnCl_2YbCl_3$ NPs confirms these elements as dopants and as constituents of the

perovskite framework on post-synthetic treatment of $CsPbBr_3$ NPs with $MnCl_2$ and $YbCl_3$ (note the core level shifts in the Yb 4d spectra in the doped NPs when compared to the $YbCl_3$ salt, **see Figure S2**). The stoichiometric ratios of the elements were calculated from the energy dispersive X-ray spectra (EDS) of the $CsPbBr_3$ and $CsPbBr_3/MnCl_2YbCl_3$ NPs (**see Table 1, Table S1 and Figure S3**). The EDS of the $CsPbBr_3/MnCl_2YbCl_3$ NPs display the signatures of the Mn and Yb along with those of the constituent Cs, Pb, Cl, and Br and corroborate the XPS data. For the $CsPbBr_3$ NPs, the Cs : Pb ratio is almost 1 : 1 while the $CsPbBr_3/MnCl_2YbCl_3$ NPs show an amount of Cs ≈ Pb + Mn + Yb. These comparisons imply that the decrease in the amount of Pb is proportional to the increase in the amount of dopants (in this case Mn and Yb) thereby indicating a substitutional displacement of the Pb^{2+} with the Mn^{2+} and Yb^{3+}.

Table 1. Stoichiometric ratio of the elements before and after the HEMCE reaction is shown[a]

Sample	**Cs**	**Pb**	**Mn**	**Yb**
$CsPbBr_3$	1.0	1.1	-	-
$CsPbBr_3/MnCl_2YbCl_3$	1.0	0.3	0.5	0.5
$CsPbCl_3$	1.0	0.9	-	-
$CsPbCl_3/MnCl_2YbCl_3$	1.0	0.8	0.3	0.2
	Cs	**Pb**	**Eu**	**Tb**
$CsPbCl_3/EuCl_3TbCl_3$	1.0	0.4	0.4	0.4

The error in determining the stoichiometry is ~15%.

Optical spectroscopy experiments were performed to analyze the photophysical properties of the $CsPbBr_3$ NPs and the $CsPbBr_3/MnCl_2YbCl_3$ NPs. The UV-vis absorption and steady-state emission spectra of the $CsPbBr_3$ NPs are shown in **Figure 2a** with an absorption and emission maximum for the first excitonic transition at 484 nm and 494 nm respectively. The quantum yield of the $CsPbBr_3$ NPs was found to be 60% with an average emission lifetime of 2.44 ns (**see Figure S4 and Table S2**). The ion exchange induced by co-adding $MnCl_2$ and $YbCl_3$ salts to the $CsPbBr_3$ NPs replaces Br with the Cl and blue shifts the first exciton maxima of the absorption and emission to 415 nm and 424 nm respectively in the $CsPbBr_3/MnCl_2YbCl_3$ NPs (**see Figure 2c**).[10, 25] The

absorption and emission spectra of the $CsPbBr_3/MnCl_2YbCl_3$ NPs however do not overlap with those of the $CsPbCl_3$ NPs (having an exciton absorption band at 394 nm and emission at 404 nm, **Figure 2b**) owing to an incomplete halide exchange and corroborates the observations of the XRD and XPS experiments.

The $CsPbBr_3/MnCl_2YbCl_3$ NPs have an exciton emission quantum yield of 2% with an average lifetime of 0.98 ns (**see Figure S4 and Table S2**). The steady-state emission spectra of the $CsPbBr_3/MnCl_2YbCl_3$ NPs in addition to the perovskite exciton emission at 424 nm, also display emission bands centered at 610 nm and at 980 nm (**see Figure 2c**). The emission band centered at 610 nm originates from the $^4T_1 \rightarrow {}^6A_1$ transition of Mn^{2+} (having a quantum yield of 6% and an average lifetime of 940 μs, **see Figure S5 and Table S3**) while the emission band centered at 980 nm originates from the $^2F_{5/2} \rightarrow {}^2F_{7/2}$ transition of Yb^{3+} (with a quantum yield of 1.7% and an average lifetime of 490 μs **see Figure S5 and Table S3**).[24] The excitation spectra (**see Figure 2d**) generated by monitoring the emissions at 610 nm and 980 nm show a significant overlap with the absorption spectra of the $CsPbBr_3/MnCl_2YbCl_3$ NPs (**Figure 2c**) and the excitation spectrum generated by monitoring the perovskite emission band at 424 nm. These observations indicate the operation of an optical antenna effect[14] where the energy migration from the $CsPbBr_3/MnCl_2YbCl_3$ perovskite's excited exciton feeds the accepting levels of Mn^{2+} and Yb^{3+} and generates Mn^{2+*} and Yb^{3+*} emission. Optically pumping the $CsPbBr_3/MnCl_2YbCl_3$ NPs with a single excitation wavelength therefore results in three distinct emission transitions in concert spanning the UV, visible (orange-red), and NIR spectral region. The operation of host-sensitization is of critical importance since the direct optical excitation between electronic states having the same parity (as d–d and f–f transitions in Mn^{2+} and the Ln^{3+} respectively) are forbidden by Laporte selection rule and is inefficient.[36] The results of the TEM, XRD, XPS, and optical

spectroscopy experiments unequivocally prove the successful doping and incorporation of the Mn^{2+} and Yb^{3+} in the perovskite framework.

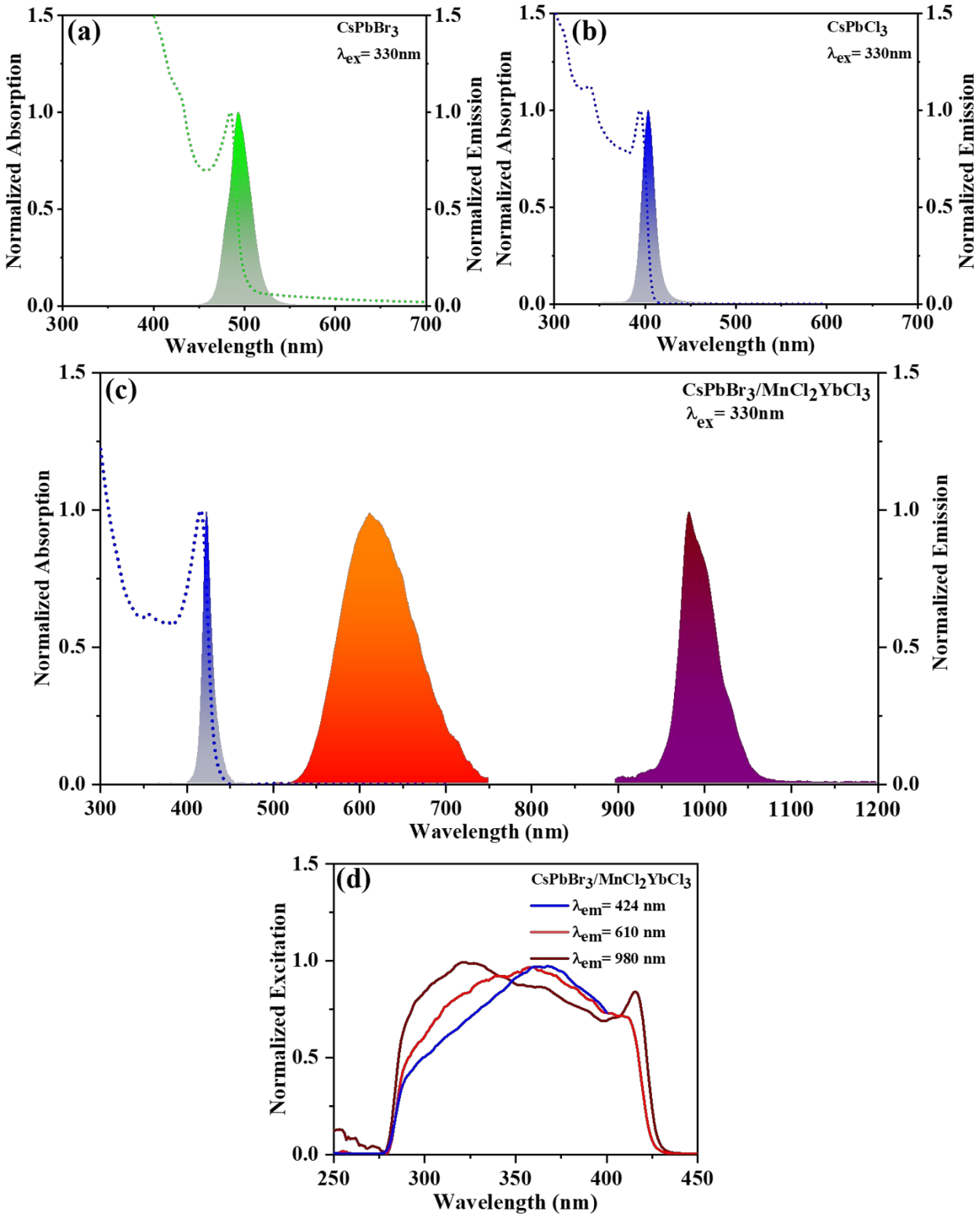

Figure 2. UV-visible absorption and steady-state emission spectra of (a) $CsPbBr_3$ NPs, (b) $CsPbCl_3$ NPs, and (c) $CsPbBr_3/MnCl_2YbCl_3$ NPs are shown along with (d) the steady-state excitation spectra of $CsPbBr_3/MnCl_2YbCl_3$ NPs. The NPs were dispersed in toluene.

The Role of Host Anion in HEMCE and Co-doping

In order to evaluate the effect of the perovskite (host) anion in controlling the HEMCE reaction, the subsequent co-doping, and the realization of sensitized dopant emission, $CsPbCl_3$ NPs were treated with $MnCl_2$ and $YbCl_3$ salts post-synthetically (see Experimental Section). **Figure 3 a-b** shows the HRTEM image of the $CsPbCl_3$ NPs before and after treatment with $MnCl_2$ and $YbCl_3$. The $CsPbCl_3$ and the $CsPbCl_3/MnCl_2YbCl_3$ NPs display identical d-spacings of 0.28 nm and 0.39 nm corresponding to the (200) and (110) planes of cubic $CsPbCl_3$ along with the retention of cubic morphology post exchange. The average nanocube edge length however changes from 7.3 ± 0.5 nm in $CsPbCl_3$ NPs to 8.3 ± 0.4 nm in $CsPbCl_3/MnCl_2YbCl_3$ NPs (**see Figure S6**). The XRD patterns of the $CsPbCl_3$ NPs and the $CsPbCl_3/MnCl_2YbCl_3$ NPs (**Figure 3c-d**) overlap with the (hkl) values at $2\theta = 15.8^o$, 22.4^o, 31.9^o, 35.8^o, 39.3^o, 45.7^o, and 48.7^o which correlate to the (100), (110), (200), (210), (211), (220), and (221) planes of cubic $CsPbCl_3$ (PDF: 01-073-0692).[25] A comparison of the Cs 3d and Pb 4f XPS signatures between $CsPbCl_3$ NPs and the $CsPbCl_3/MnCl_2YbCl_3$ NPs is shown in **Figure 3e-f**. A modest core level shift in the Pb $4f_{5/2}$ and $4f_{7/2}$ doublet of $CsPbCl_3/MnCl_2YbCl_3$ NPs (as indicated by dotted lines) shows a change in the electron density.[25, 31] The Cl 2p photoelectron signature of $CsPbCl_3$ NPs is shown in **Figure 3g**. The Mn 2p and Yb 4d XPS features (**Figure 3h-i**) in $CsPbCl_3/MnCl_2YbCl_3$ NPs shows that a change in the host NP halide (from $CsPbBr_3$ to $CsPbCl_3$) does not limit the HEMCE reaction. The core level shifts in the Mn 2p and Yb 4d XPS in the $CsPbCl_3/MnCl_2YbCl_3$ NPs when compared to the $MnCl_2$ and $YbCl_3$ salts (**see Figure S7**) further support an accurate calibration of the photoelectron yield and doping of these ions in the NPs. The stoichiometric ratio of the elements

also indicates a substitutional displacement of the Pb^{2+} by Mn^{2+} and Yb^{3+} for $CsPbCl_3/MnCl_2YbCl_3$ NPs much like the $CsPbBr_3/MnCl_2YbCl_3$ NPs (**see Table 1, Table S1 and Figure S8**).

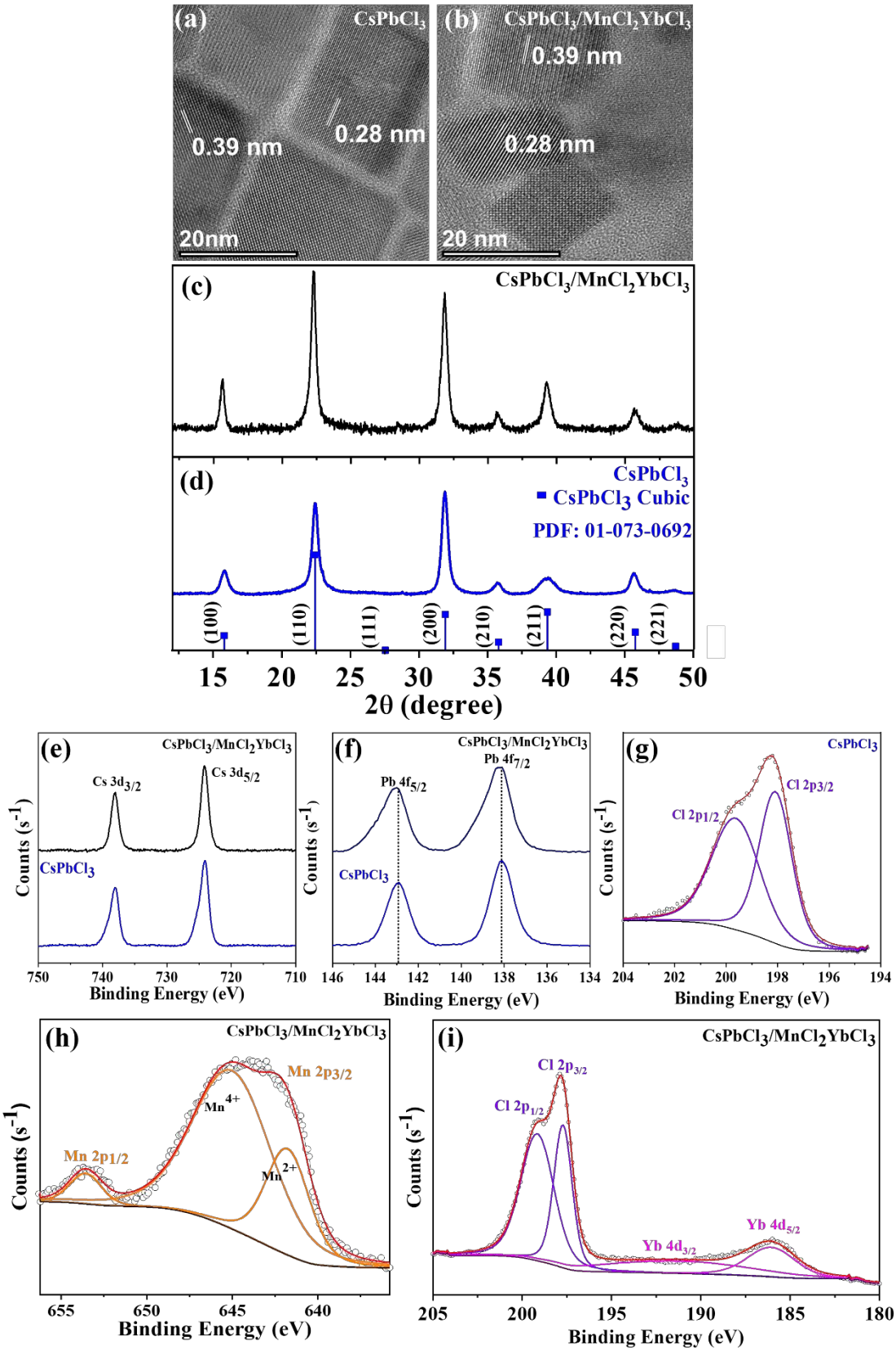
(a)
CsPbCl3
0.39 nm
0.28 nm
20nm
(b)
CsPbCl3/MnCl2YbCl3
0.39 nm
0.28 nm
20 nm
(c)
CsPbCl3/MnCl2YbCl3
(d)
CsPbCl3
CsPbCl3 Cubic
PDF: 01-073-0692
(100)
(110)
(111)
(200)
(210)
(211)
(220)
(221)
15 20 25 30 35 40 45 50
2θ (degree)
(e)
CsPbCl3/MnCl2YbCl3
Cs 3d3/2
Cs 3d5/2
CsPbCl3
Counts (s-1)
750 740 730 720 710
Binding Energy (eV)
(f)
CsPbCl3/MnCl2YbCl3
Pb 4f7/2
Pb 4f5/2
CsPbCl3
Counts (s-1)
146 144 142 140 138 136 134
Binding Energy (eV)
(g)
CsPbCl3
Cl 2p3/2
Cl 2p1/2
Counts (s-1)
204 202 200 198 196 194
Binding Energy (eV)
(h)
CsPbCl3/MnCl2YbCl3
Mn 2p3/2
Mn4+
Mn2+
Mn 2p1/2
Counts (s-1)
655 650 645 640
Binding Energy (eV)
(i)
CsPbCl3/MnCl2YbCl3
Cl 2p3/2
Cl 2p1/2
Yb 4d5/2
Yb 4d3/2
Counts (s-1)
205 200 195 190 185 180
Binding Energy (eV)

Figure 3. High-resolution TEM images of the (a) $CsPbCl_3$ and (b) $CsPbCl_3/MnCl_2YbCl_3$ NPs are shown along with XRD patterns of the (c) $CsPbCl_3$ (blue) and (d) $CsPbBr_3/MnCl_2YbCl_3$ NPs (black). The powder diffraction files (PDF) of cubic $CsPbCl_3$ are also presented to facilitate appropriate comparison. XPS data of (e) Cs 3d and (f) Pb 4f of $CsPbCl_3$ (blue) and $CsPbCl_3/MnCl_2YbCl_3$ NPs (black) are shown along with (g) Cl 2p spectra (fitted in violet) of the $CsPbCl_3$ NPs. The XPS of (h) Mn 2p (fitted in orange) and (i) Yb 4d (fitted in magenta) along with Cl 2p (fitted in violet) are shown in panel (i) for the $CsPbCl_3/MnCl_2YbCl_3$ NPs. Through panels (g-i), the spectra are presented as black circles while the envelope of the fit is shown with a red line.

The UV-visible absorption and steady-state emission spectra of the $CsPbCl_3/MnCl_2YbCl_3$ NPs show exciton absorption and emission maxima at 404 nm and 410 nm respectively and are red shifted when compared to the excitonic absorption and emission maxima of $CsPbCl_3$ NPs at 394 nm and 404 nm (**Figure 4 a,c**).[16, 25] This doping induced increase in the exciton absorption and emission maxima corroborates the increase in the average edge length of the $CsPbCl_3/MnCl_2YbCl_3$ nanocubes (*vide supra*). The $CsPbCl_3$ NPs have an exciton emission quantum yield of 1.2% with an average emission lifetime of 1.33 ns while the $CsPbCl_3/MnCl_2YbCl_3$ NPs display perovskite emission quantum yield of 1.6% and an average emission lifetime of 1.50 ns (**see Figure S9 and Table S2**). This modest increase in the $CsPbCl_3/MnCl_2YbCl_3$ quantum yield and lifetime is attributed to the passivation of the $CsPbCl_3$ surface defects[25] owing to an increase in NP dimension and Mn^{2+} and Yb^{3+} incorporation. The $CsPbCl_3/MnCl_2YbCl_3$ NPs act as a viable host to sensitize Mn^{2+} and Yb^{3+} emission as seen in **Figure 4 b-c**. In addition to the perovskite emission, excitation of the NPs at 330 nm results in the realization of Mn^{2+} emission centered at 610 nm (corresponding to the $^4T_1 \rightarrow {}^6A_1$ transition) with a quantum yield of 6.2% and an average Mn^{2+} emission lifetime of 920 μs (**see Figure S10 and Table S3**) and Yb^{3+} emission centered at 980 nm (corresponding to the $^2F_{5/2} \rightarrow {}^2F_{7/2}$ transition) with a quantum yield of 1% and an average lifetime of 680 μs.[16, 24] The steady-state excitation spectra generated by monitoring the Mn^{2+} emission at 610 nm and Yb^{3+} emission at 980 nm show

a significant overlap with the absorption spectra of the $CsPbCl_3/MnCl_2YbCl_3$ NPs and the excitation spectra generated by monitoring the perovskite emission band at 410 nm, thereby confirming the operation of host sensitization. The structural characterization data and the results of the optical spectroscopy experiments prove that $CsPbCl_3$ NPs can readily undergo HEMCE reaction and can be used to co-dope Mn^{2+} and Yb^{3+} ions, thereby generating the optically active $CsPbCl_3/MnCl_2YbCl_3$ NPs with host-sensitized multicolor dopant(s) emission.

The ability of $CsPbCl_3$ NPs to incorporate a different set of optically active dopant combination was tested by treating the NPs with $EuCl_3$ and $TbCl_3$ salts (see Experimental section) which resulted in the generation of $CsPbCl_3/EuCl_3TbCl_3$ NPs. Like the $CsPbCl_3/MnCl_2YbCl_3$ NPs, the $CsPbCl_3/EuCl_3TbCl_3$ NPs retain the cubic $CsPbCl_3$ crystal structure (**see Figure S11**) and show a substitutional displacement of Pb^{2+} by Eu^{3+} and Tb^{3+} (**see Table 1, Table S1, Figure S12**). The UV-visible absorption and steady-state emission spectra of the $CsPbCl_3/EuCl_3TbCl_3$ NPs are shown in **Figure S13**. It must be noted that due to the large difference in the radiative rate of the perovskite emission (which is typically in the nanoseconds time scale) and the Ln^{3+} emission (typically in the range of microseconds to milliseconds), the intense perovskite emission can sometimes mask the Ln^{3+} emission in steady-state (**see Figure S13**).[25] The ideal modality of visualizing Ln^{3+} emission can be achieved by a time-gated spectral acquisition where a delay time removes the nanosecond lived components and a gate time allows the collection of microsecond-millisecond lived species.[14, 25] **Figure 4d** shows the time-gated excitation and emission spectra of the $CsPbCl_3/EuCl_3TbCl_3$ NPs. Exciting the NPs at 330 nm shows sharp Tb^{3+} and Eu^{3+} emission bands. The emission bands at 490 nm and 547 nm are characteristic of the $^5D_4 \rightarrow {}^7F_6$ and $^5D_4 \rightarrow {}^7F_5$ transitions of Tb^{3+}.[37] The emission bands at 593 nm, 616 nm, 653 nm, and 700 nm correspond to the $^5D_0 \rightarrow {}^7F_J$ (J = 1, 2, 3, 4) transitions of the Eu^{3+}.[37] It is worth mentioning that the Eu^{3+}

emission band at 593 nm may have some contribution from the $^5D_4 \rightarrow {}^7F_4$ transition of Tb^{3+} (which is usually centered at 585 nm).[38] The identical features of the excitation spectra generated on monitoring the emission bands at 616 nm and 700 nm confirms their Eu^{3+} centric origin and differs from the excitation spectrum generated by monitoring the Tb^{3+} emission band at 545 nm. The broad excitation spectra largely indicate the operation of host sensitization in realizing the Tb^{3+} and Eu^{3+} emission, although contributions from Tb^{3+} and Eu^{3+} direct excitation lines are also visible. The most intense Tb^{3+} emission transition (at 545 nm) is 2.4 times lower than that of the Eu^{3+} emission transition (at 616 nm), even though their average emission lifetimes differ by only 1.5 times (Tb^{3+} emission lifetime is 180 μs and Eu^{3+} emission lifetime is 270 μs - see **Figure S14** and **Table S4**) and the doping levels in $CsPbCl_3/EuCl_3TbCl_3$ NPs (**Table 1 and Table S1**) are nearly identical. A sensitization mechanism that accounts for these trends is discussed later (*vide infra*). The broad excitation spectra generated by monitoring the Ln^{3+} (Ln^{3+} = Eu, Tb) emission bands (as opposed to the sharp excitation lines of the Ln^{3+} salts, **see Figure S15**)[14] and the non-monoexponential nature of their lifetime decays is a clear signature for the successful incorporation of the Ln^{3+} in a host NP.[14]

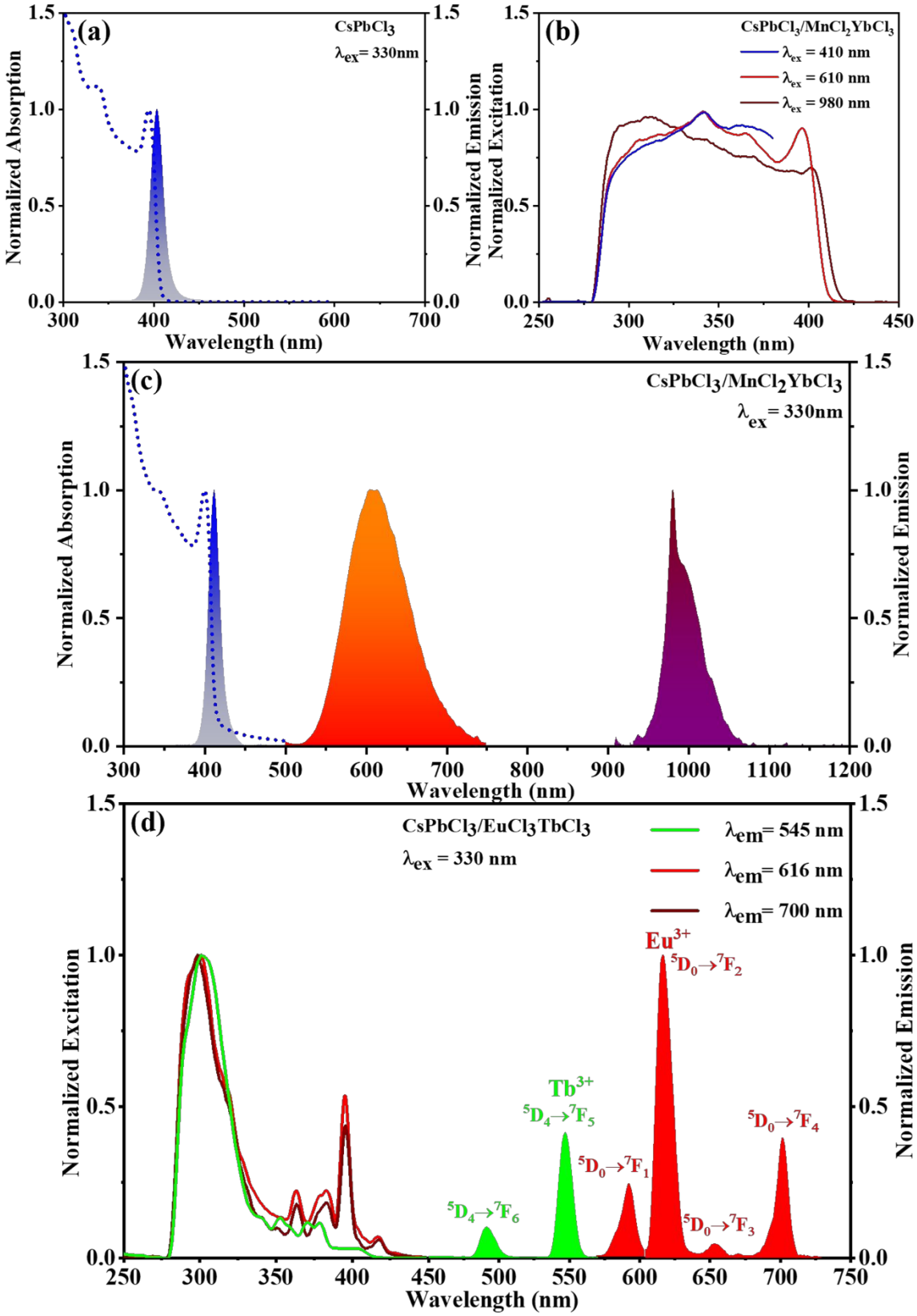
(a)
CsPbCl3
λex= 330nm
Normalized Absorption
Wavelength (nm)
(b)
CsPbCl3/MnCl2YbCl3
λex = 410 nm
λex = 610 nm
λex = 980 nm
Normalized Emission
Normalized Excitation
Wavelength (nm)
(c)
CsPbCl3/MnCl2YbCl3
λex= 330nm
Normalized Absorption
Normalized Emission
Wavelength (nm)
(d)
CsPbCl3/EuCl3TbCl3
λex = 330 nm
λem= 545 nm
λem= 616 nm
λem= 700 nm
Eu3+
5D0→7F2
Tb3+
5D4→7F5
5D0→7F1
5D0→7F4
5D4→7F6
5D0→7F3
Normalized Excitation
Normalized Emission
Wavelength (nm)

Figure 4. (a) UV-vis absorption and emission spectra of the $CsPbCl_3$ NPs, (b-c) steady-state excitation, emission, and absorption spectra of the $CsPbCl_3/MnCl_2YbCl_3$ NPs and (d) time-gated excitation and emission spectra of $CsPbCl_3/EuCl_3TbCl_3$ NPs are shown. The NPs were dispersed in toluene for acquiring the spectra.

Band Edge Considerations

Charge trapping, or co-localization, as a mechanism to explain dopant sensitization is widely used for defects in bulk semiconductors and finds precedence in perovskites too.[39-45] We have proposed a charge trapping mediated model, where identifying and placing the dopant ground and luminescent energy levels appropriately with respect to the band edges of the host NP rationalizes the observed sensitization efficiency of the dopants for a range of semiconductor hosts.[14] We have shown this approach to be particularly effective in rationalizing the observed Ln^{3+} luminescence in II-VI sulfide,[46] selenide,[23] and IV-VI oxide[47-51] semiconductor NPs in singly doped and co-doped systems. The dynamics of inter-Ln energy transfer in co-doped systems also finds appropriate explanation within this charge trapping mechanism.[38, 50] Additionally, we have shown that spectral overlap mediated energy migration is a poor predictor of dopant sensitization in II-VI semiconductor NPs, metal oxide NPs, and $CsPbX_3$ NPs.[14, 25, 52]

Figure 5 presents an energy level schematic of the $CsPbCl_3/MnCl_2YbCl_3$ and $CsPbCl_3/EuCl_3TbCl_3$ NPs. The Mn^{2+} ground ($^6A_1$) and luminescent ($^4T_1$) energy levels were placed according to the recent computational study by De Angelis and coworkers,[53] in which they posit that a charge trapping mechanism circumvents the spin and orbital restrictions arising from other mechanisms, making it a preferred pathway to explain Mn^{2+} emission in $CsPbCl_3$ NPs. The energy diagram assumes the bandgap of the $CsPbCl_3$ NPs to be 3.15 eV and places the zero of the energy scale at the valence band edge. The $^6A_1$ energy level is placed 3.0 eV below the valence band.[53] The known energy difference of 2.05 eV between the $^4T_1$ and $^6A_1$ levels of Mn(II), for $CsPbCl_3$, places the $^4T_1$ level 0.95 eV below the valence band.[53]

The placement of the Ln^{3+} [Ln^{3+} = Eu, Tb, and Yb] ground and luminescent energy levels is adapted from the reports of Dorenbos and coworkers[54, 55] and is based on the following guidelines:

(i) The binding energies of the Ln^{3+} follow a universal trend due to their core-like nature and are independent of the host.

(ii) The charge transfer energy (E_{CT}) from the anion valence band to the Eu^{3+} is equal to the energy difference between the valence band of the host and the Eu^{2+} ground state.

(iii) The energy difference between the Eu^{3+} and the Eu^{2+} ground energy level is ~5.7 eV for lower bandgap materials.

A way to estimate the E_{CT} for systems where experimental determination is difficult (as is the case here) is to use Pauling's electronegativity (η) scale and Jørgensen's relationship[56] according to the equation:

$$E_{CT} = 3.72\ (\eta - 2)\ \text{eV} \quad (1)$$

An average electronegativity of Cl and Pb was used to estimate the E_{CT} (2.77 eV) since the valence band in $CsPbCl_3$ has contributions from both Cl 3p and Pb 6s orbitals. The Eu^{2+} ground state was then placed at 2.77 eV which then helps place the other Ln^{2+} and Ln^{3+} ground states.

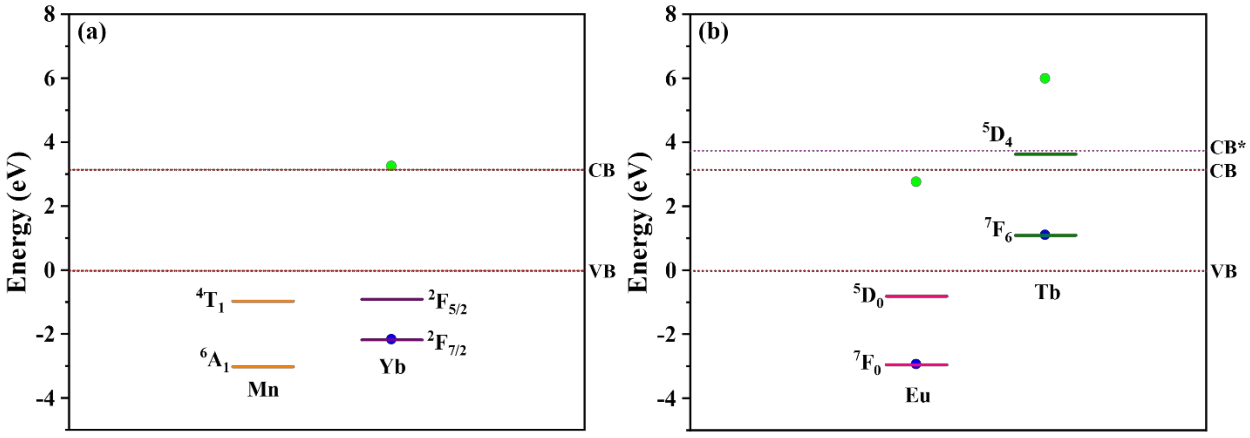

Figure 5. The relative energy levels of the ground and luminescent energy levels of Mn^{2+} (orange), Yb^{3+} (purple) (panel a) and Eu^{3+} (pink), Tb^{3+} (olive) (panel b) with respect to the valence (VB) and conduction (CB) band (red) of a $CsPbCl_3$ host is shown. The blue and green circles represent the Ln^{3+} and Ln^{2+} (Ln = Eu, Tb, and Yb) ground states respectively.

For the $CsPbCl_3/MnCl_2YbCl_3$ NPs (**Figure 5a**), optical excitation of the host results in the generation of an electron-hole pair. The Mn^{2+} $^6A_1$ and the Yb^{3+} $^2F_{7/2}$ ground states (GS) are positioned to be appropriate hole traps while the Mn^{2+} and Yb^{3+} luminescent states (LS) i.e. $^4T_1$ and $^2F_{5/2}$ respectively act as electron traps. Recombination of the electron-hole pair at these trap states results in the population of the excited Mn^{2+*} and Yb^{3+*} states and realization of sensitized Mn^{2+} and Yb^{3+} emission.

The Eu^{3+} $^7F_0$ and $^5D_0$ states (**see Figure 5b**) act as hole and electron traps respectively, and nonradiative recombination of the electron-hole pair in these trap states populates the Eu^{3+*} state leading to sensitized Eu^{3+} emission, much like the Mn and Yb cases. The Tb^{3+} $^7F_6$ is placed 1.11 eV above the valence band and acts as an effective hole trap but the $^5D_4$ level is situated 0.49 eV above the conduction band and autoionization processes should reduce the Tb^{3+} emission. The presence of a higher energy absorption band at 300-310 nm in the time-gated excitation spectra of the $CsPbCl_3/EuCl_3YbCl_3$ NPs, which also appears in the absorption spectrum, correlates with a higher energy perovskite excited state, with contributions from Tb^{3+}4f-5d energy transitions, and

is shown as CB* in **Figure 5b**.[25,27] The placement of CB* makes the $^5D_4$ level a moderate-weak electron trap for higher energy excitations and explains the realization of Tb^{3+} emission. In addition to these considerations, $Tb^{3+} \rightarrow Eu^{3+}$ energy transfer (which is well established in molecular complexes[57, 58] and in semiconductor NPs[38]) also becomes a viable process.

Conclusion

This study presents a post-synthetic ion exchange strategy to introduce two distinct emitters Mn^{2+} and Yb^{3+} in $CsPbX_3$ NPs in the quest to generate multicolor emission. Co-addition of $MnCl_2$ and $YbCl_3$ salts to the $CsPbBr_3$ results in a halide exchange and the substitutional replacement of Pb^{2+} with Mn^{2+} and Yb^{3+} to generate the corresponding $CsPbBr_3/MnCl_2YbCl_3$ NPs. The effect of host halide in controlling the ion exchange reaction was judged by treating $CsPbCl_3$ NPs with $MnCl_2$ and $YbCl_3$ salts. While the transformation of $CsPbBr_3$ to $CsPbBr_3/MnCl_2YbCl_3$ NPs involves a change in crystal structure with a retention of the NP morphology and dimension, the conversion of $CsPbCl_3$ NPs to $CsPbCl_3/EuCl_3YbCl_3$ NPs maintains the crystal structure but changes the NP dimension. Both the $CsPbBr_3/MnCl_2YbCl_3$ and $CsPbCl_3/EuCl_3YbCl_3$ NPs display the perovskite emission and host sensitized Mn^{2+} and Yb^{3+} emission, which gives rise to a material that spans the UV, visible, and NIR spectral region. With $CsPbCl_3$ as a model system, the possibility of introducing a different set of co-dopants was tested with Eu^{3+} and Tb^{3+}. The placement of dopant energy levels with respect to the $CsPbCl_3$ NP band edges and their implications for the realization of sensitized multi-dopant emission and the energy migration pathways are discussed and underscore the utility of rational design principles to prepare perovskite-dopant(s) combination for predictable dopant(s) emission.

Experimental Section

Materials

Cesium carbonate (Cs_2CO_3, 99.9% trace metals basis), lead(II) bromide ($PbBr_2$, 99.999% trace metals basis), and ytterbium(III) chloride ($YbCl_3$, anhydrous, 99.9%) were purchased from Alfa Aesar. Lead(II) chloride ($PbCl_2$, 99.999% trace metals basis), manganese(II) chloride ($MnCl_2$, 99+%, anhydrous, -80 mesh), europium(III) chloride hexahydrate ($EuCl_3.6H_2O$, 99.99% trace metals basis), terbium(III) chloride hexahydrate ($TbCl_3.6H_2O$, 99.99% trace metals basis), N, N-dimethylformamide (DMF, anhydrous, 99.8%), and octadecene (ODE, 90%) were purchased from Sigma Aldrich. Oleic acid (OA, extrapure, 65%), oleylamine (OAm, pure, 96%), toluene (99%), and ethyl acetate (99%) were purchased from Sisco Research Laboratories. All chemicals were used without further purification.

Synthesis of Cesium Oleate (Cs-oleate)

Typically, 0.407g Cs_2CO_3, 1.25 ml OA and 20 ml ODE were added to a three-neck round bottomed (RB) flask. The mixture was first degassed under vacuum and heated for 1 hour at 120 °C. The reaction mixture was then sealed in a nitrogen atmosphere and the temperature was raised to 150 °C for the complete dissolution of Cs_2CO_3 to form Cs-oleate.

Synthesis of $CsPbBr_3$ NPs

The synthesis of $CsPbBr_3$ NPs was adapted from the report of Kovalenko and coworkers[9] with modifications. Briefly, 280 mg $PbBr_2$ and 20 ml ODE were loaded in a three neck RB flask and put under vacuum for 1 h at 120 °C and then sealed in a nitrogen atmosphere. A 1:1 ratio of OAm:OA (2 ml of each) was then injected into the reaction mixture and the temperature was raised to 140 °C. The reaction was allowed to continue until the complete dissolution of $PbBr_2$. 2 ml Cs-oleate was then rapidly injected and the reaction was quenched after 10 seconds by cooling the

flask in an ice bath. The crude reaction mixture was then centrifuged at 6500 rpm and 4 °C for 15 minutes. The supernatant was collected and a 1:1 volume/volume ratio of ethyl acetate was added and then centrifuged at 8000 rpm for 10 min. The obtained precipitate was used for further experiments.

Synthesis of $CsPbCl_3$ NPs

The synthesis of $CsPbCl_3$ NPs was also adapted from the report by Meijerink and coworkers[16] with modifications. Typically, 280 mg $PbCl_2$ and 20 ml ODE were loaded in a three neck RB flask and put under put under vacuum for 1 h at 120 °C and then sealed in a nitrogen atmosphere. A 1:1 ratio of OAm:OA (2 ml of each) was then injected into the reaction mixture and the temperature was raised to 190 °C. The reaction was allowed to continue until the complete dissolution of $PbCl_2$. Two ml Cs-oleate was then rapidly injected and the reaction was quenched immediately by cooling the flask in an ice bath. The synthesized $CsPbCl_3$ NPs were purified by centrifuging the crude reaction mixture at 8000 rpm for 20 minutes. The obtained precipitate was used for further experiments.

Post-synthetic Co-doping of Mn^{2+}– Yb^{3+} and Eu^{3+}– Tb^{3+} in Perovskite NPs

$CsPbBr_3$ NP dispersions in toluene were prepared with an optical density (O.D.) ≈ 0.8 at the first excitonic transition (485–490 nm). Next, a 40 mM $MnCl_2$ and $YbCl_3$ solution in anhydrous DMF was prepared. 0.125 ml of $MnCl_2$ and $YbCl_3$ solutions respectively were added to the 3.5 ml $CsPbBr_3$ NP dispersion and incubated overnight at room temperature. The doped NPs were purified by centrifuging at 8000 rpm for 10 minutes. The precipitate was dispersed in toluene and used for further experiments. A similar procedure was followed for doping Mn^{2+} and Yb^{3+} in $CsPbCl_3$ NPs. For co-doping Eu^{3+}–Tb^{3+} in $CsPbCl_3$ NPs, the $EuCl_3.6H_2O$ and $TbCl_3.6H_2O$ salts were used keeping the other reaction parameters unchanged.

UV-visible Absorption and UV-visible-NIR Emission Spectroscopy

UV-visible absorption spectra were collected using Shimadzu UV-1800 spectrometer. UV, visible and NIR steady-state excitation and emission spectra were collected using a FLS 1000 photoluminescence spectrometer from Edinburgh Instruments with an integration time of 1s and a spectral resolution of 1 nm and 3 nm for the visible and NIR spectral regions respectively. The excitation and emission spectra were corrected for lamp and detector response respectively. The absolute emission quantum yields were determined using the integrating sphere accessory in FLS1000. All experiments were performed at room temperature.

Time-gated excitation and emission spectra were also collected using the FLS 1000 photoluminescence spectrometer from Edinburgh Instruments using a microsecond flash lamp with a delay time of 50 μs and a detection window of 5 ms.

Time-resolved Luminescence Spectroscopy

The time-resolved emission decay profiles of the NPs were collected using the time-correlated single photon counting (TCSPC) method with FLS 1000 TCSPC module (Edinburgh Instruments). The samples were excited using a picosecond pulsed diode laser at 405 nm with a repetition rate of 1MHz and the emission was collected at the magic angle. The full-width-at-half-maximum (FWHM) of the instrument response function (IRF) was ≤600 ps.

The Mn^{2+}, Yb^{3+}, Eu^{3+}, and Tb^{3+} emission decays were collected using a multichannel scaling (MCS) photon counting method using a microsecond flashlamp with a repetition rate of 20Hz. The decays were fitted using Fluoracle and FAST software from Edinburgh Instruments.

X-ray Diffraction (XRD)

Powder XRD patterns were collected from a Rigaku Ultima IV X-Ray diffractometer operated with an X-ray generator voltage and current of 50 kV and 60 mA respectively and using a Cu Kα

source (λ =1.54187 Å). Concentrated NP dispersions were drop-cast on a clean glass substrate and then dried before acquiring the spectra at room temperature. Data analysis was performed with the Rigaku PDXL data processing software.

Electron Microscopy

The transmission electron microscope (TEM) images were acquired using Thermofisher Talos F200 S operated at an acceleration potential of 200 kV. The samples were prepared by drop-casting a 10 µl NP dispersion in toluene onto a Cu TEM grid with ultra-thin carbon supporting film and dried in air. The stoichiometric ratio of the different elements in the NPs before and after exchange was determined using the energy dispersive X-ray spectroscopy (EDS) on the JEOL JSM-7100F field emission scanning electron microscope (SEM). The samples were prepared by drop-casting NP dispersions in toluene onto a silicon wafer and air dried.

X-ray Photoelectron Spectroscopy (XPS)

XPS spectra were collected using a Thermo Fisher Scientific K-Alpha. Samples were prepared by drop-casting a concentrated NP dispersion in toluene on clean glass substrates and dried. Each spectrum was referenced to the peak energy position observed for adventitious carbon (C 1s 284.6 eV).

Associated Content

Supplementary Information

TEM images, EDS, XPS, and photoluminescence spectra, emission decays, and tables (PDF)

Conflicts of Interest

There are no conflicts of interest to declare.

Acknowledgements

J.J.P. acknowledges SERB-DST for providing a fellowship. G.H.D. acknowledges Jain University for the generous start-up grant (grant No. JU/MRP/CNMS/21/2022). D.H.W acknowledges the

U.S. Department of Energy (grant no. ER46430). R.G.B. acknowledges the Science and Engineering Research Board (SERB), Department of Science and Technology (DST) (No: SPF/2023/000066) for funding.

References

1. A. Dey, J. Ye, A. De, E. Debroye, S. K. Ha, E. Bladt, A. S. Kshirsagar, Z. Wang, J. Yin, Y. Wang, L. N. Quan, F. Yan, M. Gao, X. Li, J. Shamsi, T. Debnath, M. Cao, M. A. Scheel, S. Kumar, J. A. Steele, M. Gerhard, L. Chouhan, K. Xu, X.-g. Wu, Y. Li, Y. Zhang, A. Dutta, C. Han, I. Vincon, A. L. Rogach, A. Nag, A. Samanta, B. A. Korgel, C.-J. Shih, D. R. Gamelin, D. H. Son, H. Zeng, H. Zhong, H. Sun, H. V. Demir, I. G. Scheblykin, I. Mora-Seró, J. K. Stolarczyk, J. Z. Zhang, J. Feldmann, J. Hofkens, J. M. Luther, J. Pérez-Prieto, L. Li, L. Manna, M. I. Bodnarchuk, M. V. Kovalenko, M. B. J. Roeffaers, N. Pradhan, O. F. Mohammed, O. M. Bakr, P. Yang, P. Müller-Buschbaum, P. V. Kamat, Q. Bao, Q. Zhang, R. Krahne, R. E. Galian, S. D. Stranks, S. Bals, V. Biju, W. A. Tisdale, Y. Yan, R. L. Z. Hoye and L. Polavarapu, *ACS Nano*, 2021, **15**, 10775-10981.
2. J. Shamsi, A. S. Urban, M. Imran, L. De Trizio and L. Manna, *Chem. Rev.*, 2019, **119**, 3296-3348.
3. K. Lin, J. Xing, L. N. Quan, F. P. G. de Arquer, X. Gong, J. Lu, L. Xie, W. Zhao, D. Zhang, C. Yan, W. Li, X. Liu, Y. Lu, J. Kirman, E. H. Sargent, Q. Xiong and Z. Wei, *Nature*, 2018, **562**, 245-248.
4. Q. Zhang, Q. Shang, R. Su, T. T. H. Do and Q. Xiong, *Nano Lett.*, 2021, **21**, 1903-1914.
5. A. Ho-Baillie, M. Zhang, C. F. J. Lau, F.-J. Ma and S. Huang, *Joule*, 2019, **3**, 938-955.
6. H. Huang, M. I. Bodnarchuk, S. V. Kershaw, M. V. Kovalenko and A. L. Rogach, *ACS Energy Lett.*, 2017, **2**, 2071-2083.
7. F. Di Stasio, S. Christodoulou, N. Huo and G. Konstantatos, *Chem. Mater.*, 2017, **29**, 7663-7667.
8. J. Chen, K. Žídek, P. Chábera, D. Liu, P. Cheng, L. Nuuttila, M. J. Al-Marri, H. Lehtivuori, M. E. Messing, K. Han, K. Zheng and T. Pullerits, *J. Phys. Chem. Lett.*, 2017, **8**, 2316-2321.
9. L. Protesescu, S. Yakunin, M. I. Bodnarchuk, F. Krieg, R. Caputo, C. H. Hendon, R. X. Yang, A. Walsh and M. V. Kovalenko, *Nano Lett.*, 2015, **15**, 3692-3696.
10. Q. A. Akkerman, V. D'Innocenzo, S. Accornero, A. Scarpellini, A. Petrozza, M. Prato and L. Manna, *J. Am. Chem. Soc.*, 2015, **137**, 10276-10281.
11. Y. Dong, T. Qiao, D. Kim, D. Parobek, D. Rossi and D. H. Son, *Nano Lett.*, 2018, **18**, 3716-3722.
12. C.-H. Lu, G. V. Biesold-McGee, Y. Liu, Z. Kang and Z. Lin, *Chem. Soc. Rev.*, 2020, **49**, 4953-5007.
13. W. Liu, Q. Lin, H. Li, K. Wu, I. Robel, J. M. Pietryga and V. I. Klimov, *J. Am. Chem. Soc.*, 2016, **138**, 14954-14961.
14. G. H. Debnath, P. Mukherjee and D. H. Waldeck, *J. Phys. Chem. C*, 2020, **124**, 26495-26517.
15. G. Liu and B. Jacquier, *Spectroscopic Properties of Rare Earths in Optical Materials*, Springer Berlin Heidelberg, 2005.
16. C. C. Lin, K. Y. Xu, D. Wang and A. Meijerink, *Sci. Rep.*, 2017, **7**, 45906.

17. G. H. Debnath, S. Bhattacharya, A. Adhikary and P. Mukherjee, *New J. Chem.*, 2018, **42**, 14832-14842.
18. D. Zhou, D. Liu, G. Pan, X. Chen, D. Li, W. Xu, X. Bai and H. Song, *Adv. Mater.*, 2017, **29**, 1704149.
19. H. Shao, X. Bai, H. Cui, G. Pan, P. Jing, S. Qu, J. Zhu, Y. Zhai, B. Dong and H. Song, *Nanoscale*, 2018, **10**, 1023-1029.
20. X. Zhang, Y. Zhang, X. Zhang, W. Yin, Y. Wang, H. Wang, M. Lu, Z. Li, Z. Gu and W. W. Yu, *J. Mater. Chem. C*, 2018, **6**, 10101-10105.
21. M. Zeng, F. Locardi, D. Mara, Z. Hens, R. Van Deun and F. Artizzu, *Nanoscale*, 2021, **13**, 8118-8125.
22. P. Mukherjee, R. F. Sloan, C. M. Shade, D. H. Waldeck and S. Petoud, *J. Phys. Chem. C*, 2013, **117**, 14451-14460.
23. G. H. Debnath, S. Rudra, A. Bhattacharyya, N. Guchhait and P. Mukherjee, *Journal of Colloid and Interface Science*, 2019, **540**, 448-465.
24. W. J. Mir, Y. Mahor, A. Lohar, M. Jagadeeswararao, S. Das, S. Mahamuni and A. Nag, *Chem. Mater.*, 2018, **30**, 8170-8178.
25. G. H. Debnath, B. P. Bloom, S. Tan and D. H. Waldeck, *Nanoscale*, 2022, **14**, 6037-6051.
26. R. N. Bhargava, D. Gallagher, X. Hong and A. Nurmikko, *Phys. Rev. Lett.*, 1994, **72**, 416-419.
27. J.-C. G. Bünzli and C. Piguet, *Chem. Soc. Rev.*, 2005, **34**, 1048-1077.
28. Y. Altintas, I. Torun, A. F. Yazici, E. Beskazak, T. Erdem, M. Serdar Onses and E. Mutlugun, *Chemical Engineering Journal*, 2020, **380**, 122493.
29. Y. Zhao, Y. Xu, L. Shi and Y. Fan, *Anal. Chem.*, 2021, **93**, 11033-11042.
30. Z. Yang, J. Xu, S. Zong, S. Xu, D. Zhu, Y. Zhang, C. Chen, C. Wang, Z. Wang and Y. Cui, *ACS Appl. Mater. Interfaces*, 2019, **11**, 47671-47679.
31. V. Naresh, M.-K. Cho, P.-R. Cha and N. Lee, *ACS Appl. Nano Mater.*, 2023, **6**, 4693-4706.
32. P. Arunkumar, K. H. Gil, S. Won, S. Unithrattil, Y. H. Kim, H. J. Kim and W. B. Im, *J. Phys. Chem. Lett.*, 2017, **8**, 4161-4166.
33. Z. Yang, X. Yuan, Y. Song, M. Chen, K. Xing, S. Cao, J. Zheng and J. Zhao, *J. Phys. Chem. C*, 2023, **127**, 21227-21234.
34. Y. Zhao, C. Xie, X. Zhang, K. Matras-Postolek and P. Yang, *ACS Appl. Nano Mater.*, 2021, **4**, 6223-6230.
35. D. A. Tatarinov, A. V. Sokolova, I. D. Skurlov, D. V. Danilov, A. V. Koroleva, N. K. Kuzmenko, Y. A. Timkina, M. A. Baranov, E. V. Zhizhin, A. N. Tcypkin and A. P. Litvin, *J. Mater. Chem. C*, 2023, **11**, 5657-5666.
36. O. Laporte and W. F. Meggers, *J. Opt. Soc. Am.*, 1925, **11**, 459-463.
37. J.-C. G. Bünzli, *Chem. Rev.*, 2010, **110**, 2729-2755.
38. S. Rudra, G. H. Debnath, N. Bhunia, B. P. Bloom, D. H. Waldeck and P. Mukherjee, *J. Phys. Chem. C*, 2022, **126**, 11723-11734.
39. W. W. Anderson, *Phys. Rev.*, 1964, **136**, A556-A560.
40. N. Jing-hua, H. Rui-nian, L. Wen-lian, L. Ming-tao and Y. Tian-zhi, *J. Phys. D: Appl. Phys.*, 2006, **39**, 2357-2360.
41. T. Gregorkiewicz, D. T. X. Thao, J. M. Langer, H. H. P. T. Bekman, M. S. Bresler, J. Michel and L. C. Kimerling, *Phys. Rev. B*, 2000, **61**, 5369-5375.
42. K. Thonke, K. Pressel, G. Bohnert, A. Stapor, J. Weber, M. Moser, A. Molassioti, A. Hangleiter and F. Scholz, *Semicond. Sci. Technol.*, 1990, **5**, 1124-1131.

43. M. A. J. Klik, T. Gregorkiewicz, I. V. Bradley and J.-P. R. Wells, *Phys. Rev. Lett.*, 2002, **89**, 227401-227401-227401-227404.
44. W. J. Chang, S. Irgen-Gioro, S. Padgaonkar, R. López-Arteaga and E. A. Weiss, *J. Phys. Chem. C*, 2021, **125**, 25634-25642.
45. M. Zeng, F. Artizzu, J. Liu, S. Singh, F. Locardi, D. Mara, Z. Hens and R. Van Deun, *ACS Appl. Nano Mater.*, 2020, **3**, 4699-4707.
46. P. Mukherjee, C. M. Shade, A. M. Yingling, D. N. Lamont, D. H. Waldeck and S. Petoud, *J. Phys. Chem. A*, 2011, **115**, 4031-4041.
47. A. Chakraborty, G. H. Debnath, N. R. Saha, D. Chattopadhyay, D. H. Waldeck and P. Mukherjee, *J. Phys. Chem. C*, 2016, **120**, 23870-23882.
48. P. Manna, G. H. Debnath, D. H. Waldeck and P. Mukherjee, *J. Phys. Chem. Lett.*, 2018, **9**, 6191-6197.
49. P. Manna, A. Chakraborty, G. H. Debnath and P. Mukherjee, *J. Phys. Chem. Lett.*, 2017, **8**, 2794-2798.
50. A. Chakraborty, G. H. Debnath and P. Mukherjee, *RSC Adv.*, 2017, **7**, 40767-40778.
51. A. Chakraborty, G. H. Debnath and P. Mukherjee, *J. Lumin.*, 2018, **203**, 257-266.
52. G. H. Debnath, A. Chakraborty, A. Ghatak, M. Mandal and P. Mukherjee, *J. Phys. Chem. C*, 2015, **119**, 24132-24141.
53. D. Ricciarelli, D. Meggiolaro, P. Belanzoni, A. A. Alothman, E. Mosconi and F. De Angelis, *ACS Energy Lett.*, 2021, **6**, 1869-1878.
54. P. Dorenbos and E. van der Kolk, *Appl. Phys. Lett.*, 2006, **89**, 061122-061121-061122-061123.
55. P. Dorenbos, *J. Alloys Compd.*, 2009, **488**, 568-573.
56. C. K. Jørgensen, *Modern Aspects of Ligand Field Theory*, North-Holland, Amsterdam, 1971.
57. Q. Li, T. Li and J. Wu, *J. Phy. Chem. B*, 2001, **105**, 12293-12296.
58. T. Zhang, Z. Xu, L. Qian, F. Teng, X. R. Xu and D. L. Tao, *J. Appl. Phys.*, 2005, **98**, 063503.